A Search for New Back Contacts for CdTe Solar Cells

Prashun Gorai[a], Dmitry Krasikov[b], Sachit Grover[b], Gang Xiong[b], Wyatt K. Metzger[b], Vladan Stevanović[a]

[a] *Colorado School of Mines, Golden, CO 80401 USA*
[b] *First Solar Inc., Santa Clara, CA.*
[c] *Corresponding authors: pgorai@mines.edu, vstevano@mines.edu*

Abstract

There is widespread interest in reaching the practical efficiency of cadmium telluride (CdTe) thin-film solar cells, which suffer from significant open-circuit voltage loss due to high surface recombination velocity and Schottky barrier at the back contact. Here, we focus on back contacts in the superstrate configuration with the goal of finding new materials, that can provide improved passivation, electron reflection and hole transport properties compared to the commonly used material, ZnTe. We performed a computational search among 229 binary and ternary tetrahedrally-bonded structures using first-principles methods and transport models to evaluate critical materials design criteria, including phase stability, electronic structure, hole transport, band alignments, and p-type dopability. Through this search, we have identified several candidate materials and their alloys (AlAs, $AgAlTe_2$, $ZnGeP_2$, $ZnSiAs_2$, $CuAlTe_2$) that exhibit promising properties for back contacts. We hope these new material recommendations and associated guidelines will inspire new directions in hole transport layer design for CdTe solar cells.

1. Introduction

Cadmium Telluride (CdTe) is currently the leading thin-film photovoltaic (PV) technology on the market. While CdTe thin-film solar cells have achieved impressive conversion efficiencies of $> 22\%$,[1] there is a growing interest in the research community and industry to reach practical efficiency limits approaching 28%, which has been achieved by GaAs solar cells with a similar bandgap, while retaining market leading cost.[2, 3] There are several materials factors that limit device efficiencies, including carrier recombination in the bulk,[4, 5] grain boundaries, and interfaces.[6] Studies indicate reducing carrier recombination at the CdTe interface with the contact layers presents a significant opportunity to ultimately increase device performance beyond 25 % efficiency.[6, 7] Back contact optimization is likely to enable further improvements in device efficiencies.[8] Figure 1 shows the typical architecture of a superstrate CdTe solar cell with a transparent top (front) contact, n-type emitter, and a hole-selective back contact to p-type CdTe. The challenge of creating an optimal back-interface contact has been the goal of academic and industrial research for several decades, and is comprehensively reviewed in Refs. 9, 10, 8. Back contact interfaces are also important for perovskite and chalcogenide (e.g., CIGS) solar cell technologies.[11] Here, we focus on the materials challenge of designing electron-reflecting back contacts that serve as efficient hole transport layers in CdTe solar cells.

Commercial thin-film CdTe solar cells employ Cu-doped ZnTe (ZnTe:Cu) as the hole-selective back contact. However, ZnTe:Cu fails to passivate the back interface or form desired electron reflection to enhance performance.[3, 12] Other Cu-containing materials that have been considered as back contacts include Cu_xTe,[13] Cu_xS,[14] HgTe:Cu, CuI, CuSCN, and $Cu_xZn_{1-x}S$.[13, 14, 15] Copper is commonly used

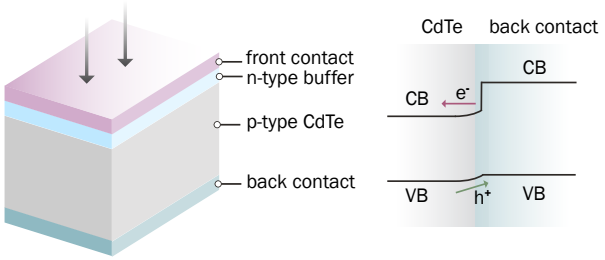

Figure 1: (left) Typical architecture of a CdTe solar cell in superstrate configuration. Arrows indicate direction of solar irradiation. (right) Desired band alignment between CdTe and the back contact, providing barrier-less hole transport and electron reflection.

to dope CdTe p-type in the $10^{14} - 10^{15}$ cm^{-3} range.[8] The Cu ions in the back contacts, including ZnTe:Cu, are known to diffuse into CdTe, and substitute Cd to form shallow acceptor states (p-type doping). However, "excess" Cu in CdTe is also associated with metastability and long-term performance degradation, including changes in the series resistance and fill factor.[16, 17, 18] Non Cu-containing compounds such as Sb_2Te_3, As_2Te_3, FeS_2, MoO_x, NiO_x, and Ni-P have also been explored for back contacts.[8] However, the realization of loss-free, electron-reflecting, hole-transport layers that form Ohmic contacts remains an outstanding materials challenge. There is a need to search for new contacts for future CdTe PV technology.

A material that is suitable as a back contact in a superstrate CdTe solar cell needs to fulfill a number of design criteria: (1) interfacial chemical stability with CdTe to prevent the formation of undesired secondary phases, (2) high hole mobility and hole-to-electron mobility ratio to facilitate hole transport away from the interface, (3) valence band (VB) alignment with CdTe, ideally within 0-0.3 eV to ensure a small barrier for hole transport (Figure 1) and robust fill factor, (4) suitable conduction band (CB) alignment to allow electron reflection at the interface, which implies higher CB minimum than CdTe (Figure 1), (5) p-type dopability, which, in addition to introducing hole carriers can also be advantageous for alignment of the Fermi energy at the interface, and (6) absence of deleterious deep interface states that cause non-radiative carrier recombination. As a candidate material will need to simultaneously satisfy this set of materials requirements. As such, the search for new back contacts for CdTe is complex and non-trivial. Since the relevant material properties can be directly estimated or inferred from first-principles calculations, a broad computational search is a starting route to find new back contacts.

Computations have proven to be a powerful tool in accelerating materials discovery beyond the conventional trial-and-error approach. With continued improvements in methods and software, and the broader availability of computational resources, high-throughput (HT) computational searches of novel functional materials have become viable. HT search approaches rely on first-principles calculations and simplified models to determine material properties and performance descriptors/metrics. To expedite searches, often various approximations are employed without overly sacrificing accuracy. In spite of the assumptions and approximations, HT computations have been quite successful in unravelling novel materials for energy storage, thermoelectrics, photovoltaics, and other applications.[19, 20]

In this work, we undertook a computational search to identify new back contacts for CdTe solar cells. We performed this search among 229 tetrahedrally-bonded structures (TBSs) from the Inorganic Crystal Structure Database (ICSD).[21] We computed the bulk and interfacial chemical stability of the TBSs. We then computed the electronic structure and estimated the hole mobility of those TBSs that satisfy the thermodynamic stability criteria. Subsequently, we assessed the band alignment of the structures that exhibit the desired band gap and hole mobility. In addition, we also considered factors such as lattice matching with CdTe, which contributes to the interfacial structure. Finally, we assessed the p-type dopability of the candidate materials with desired band alignments. From this search, we have identified several candidate TBSs and their alloys (AlAs, $AgAlTe_2$, $ZnGeP_2$, $ZnSiAs_2$, $CuAlTe_2$) that have promising properties required for back contacts in CdTe solar cells.

2. Background

Hole transport from CdTe into the back contact and therefore, solar cell device efficiency is highly sensitive to the valence band alignment Δ_{VB}.[3, 12] The electron reflection property of the back interface also critically depends on Δ_{VB} because of the associated band bending. Figure 2 shows the band schematics for the cases of negative and positive Δ_{VB}. In both cases, the conduction band edge of the back contact (BC) is higher than that of CdTe. Generally, it is understood that overly large Δ_{VB} is associated with reduced device efficiency. To quantify the tolerable range of Δ_{VB}, we performed 1-D device simulations with Solar Cell Capacitance Simulator (SCAPS)[22] for a set of representative parameters. See methods (section 6.6) for more details.

We considered valence band alignments ranging from -0.6 eV to +0.6 eV relative to the valence band edge of CdTe. For the back contact, we assumed a realistic hole doping of 10^{18} cm^{-3} and a CdTe hole mobility of 50 cm^2/Vs. Figure 7(c) summarizes the simulated device efficiency as a function of band alignment for five different scenarios where the lifetime was varied between 1-100 ns and the carrier concentration from 10^{14} cm^{-3} and 10^{15} cm^{-3} (see Table S1).

It is evident from Figure 2(c) that the device efficiency drops precipitously for large positive and negative Δ_{VB}. Specifically, within -0.4 eV $\leq \Delta_{VB} \leq$+0.3 eV, the device efficiency is practically unchanged but reduces significantly outside this range. Our device simulations are in line with the common empirical guideline that suggests $|\Delta_{VB}| \leq 0.3$ eV is tolerable.[8, 3, 12] We also considered two more scenarios to simulate: (1) an optimistic scenario of higher back contact hole doping of 10^{20} cm^{-3}, and (2) a cautious scenario of lower doping of 10^{17} cm^{-3}. Higher doping levels expand the tolerable range of valence band alignments (-0.6 eV $\leq \Delta_{VB} \leq$+0.4 eV) while lower doping levels shrink the range (-0.3 eV $\leq \Delta_{VB} \leq$+0.2 eV). In our search for new back contacts, we chose candidate materials that have the desired range of Δ_{VB} for a doping level of 10^{18} cm^{-3} (Figure 2c).

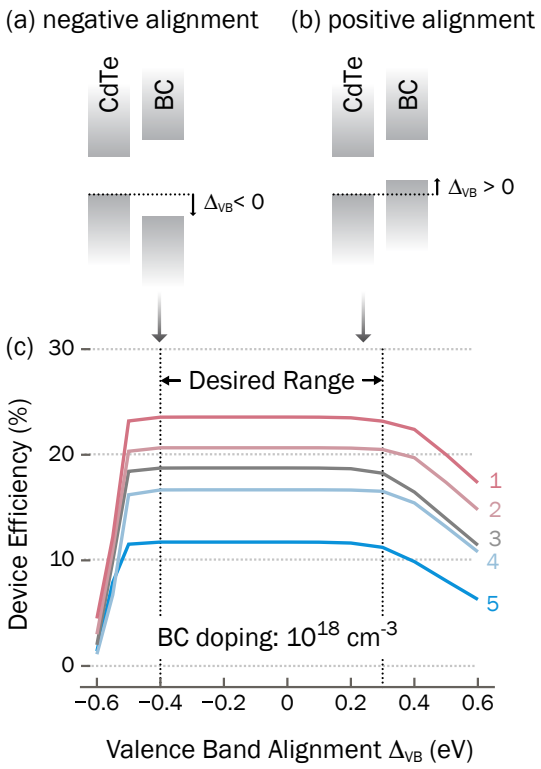

Figure 2: Schematic band alignments of CdTe and back contact (BC) for two different scenarios of valence band alignment Δ_{VB}: (a) negative, and (b) positive. The conduction band edge in both scenarios are higher in energy than CdTe. (c) Simulated solar cell device efficiency for 5 different scenarios, labelled 1-5 (see Table S1 for details) assuming *p*-type CdTe with hole concentrations of 10^{14} cm^{-3} and 10^{15} cm^{-3}, and back contact hole doping of 10^{18} cm^{-3}.

3. Results

The computational workflow employed to downselect the candidate materials is schematically presented in Figure 3. We performed the search among materials documented in the Inorganic Crystal Structure Database (ICSD). We started by first identifying ordered and stoichiometric binary and ternary compounds that have tetrahedrally-bonded structures. Next, we used the convex hull analysis to determine the bulk thermodynamic phase stability as well as the interfacial chemical stability with CdTe. We cal-

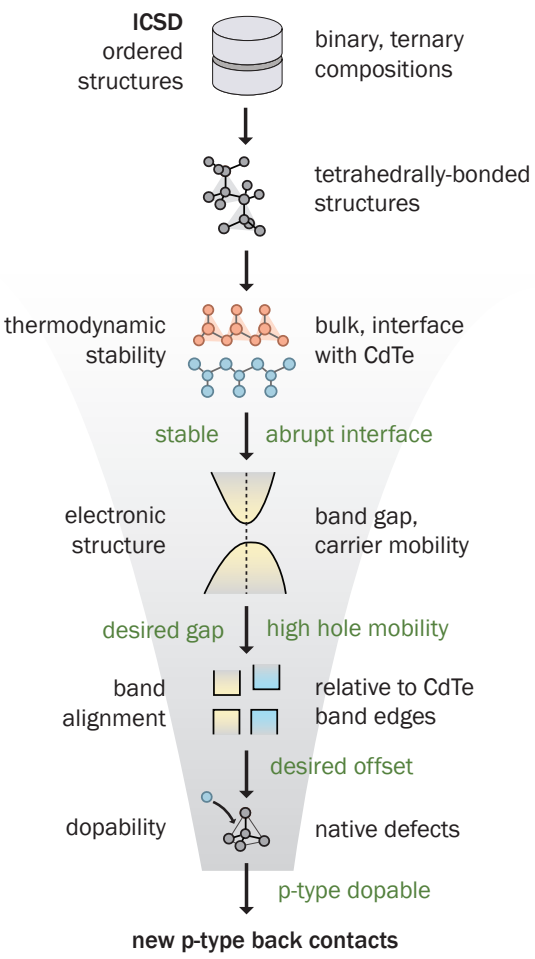

Figure 3: Schematic of the computational workflow to screen materials and identify promising candidates for back contacts in CdTe solar cells.

culated the electronic structure and hole mobility for those structures that satisfy the thermodynamic stability criteria. Materials that were predicted to have a desired band gap and relatively high hole mobility were then asssessed for their band alignment relative to CdTe. Finally, we used first-principles calculations to evaluate the p-type dopability of the candidate structures with the desired band alignments.

3.1. Tetrahedrally-bonded Structures in the ICSD

We developed an automated procedure to identify TBSs in the ICSD (see section 6.1 for details) with binary or ternary chemistries and primitive cells containing less than 50 atoms. In addition, structures containing rare-earth lanthanides (except La) and actinides were excluded for practical considerations. From this search, we identified 229 TBSs, including 144 binary and 85 ternary structures. We have verified that our automated search correctly captures well-known TBSs, including binary II-VI wurtzite (e.g., ZnO) and III-V zinc blende (e.g., GaAs) structures, and ternary I-III-VI_2 chalcopyrites (e.g., $CuInSe_2$). Using the same automated algorithm, we also confirmed the identification of quaternary I_2-II-IV-VI_4 structures such as kesterites e.g., Cu_2ZnSnS_2, and related compounds (not included in the subsequent search for reasons explained above).

3.2. Thermodynamic Bulk and Interfacial Chemical Stability

We assess the thermodynamic bulk and interfacial chemical stability (with CdTe) of the 229 TBSs from grand potential phase diagrams obtained through convex hull construction (see section 6.2 for details). Here, bulk phase stability implies that the TBS is thermodynamically stable against decomposition into competing phases. In a given chemical space, we consider all known competing phases that are documented in the ICSD. For example, to assess the bulk stability of $CuInSe_2$, all competing phases in the ternary Cu-In-Se chemical space are considered in constructing the convex hull. A structure that lies on the convex hull i.e., energy above the hull (ΔE_{hull}) is zero, is thermodynamically stable.

Next, for the TBSs that were found to be bulk stable, we assessed their interfacial chemical stability with CdTe also through convex hull construction. In this case, the convex hull is constructed by considering all the competing phases in the chemical space comprised of the elements in the TBS as well as Cd and Te. For example, to assess the interfacial chemical stability of ZnTe (Figure 4a), we consider all competing phases in the ternary Zn-Cd-Te chemical

space; ZnTe and CdTe are the only known competing phases. Here, interfacial chemical stability requires that the TBS is chemically stable in contact with CdTe under some chemical potential conditions. In a grand potential phase diagram, this requirement manifests as a shared edge between CdTe and the TBS, as shown in the case of ZnTe in Figure 4(a). In a compositional phase diagram, this is equivalent to the TBS sharing a tie line with CdTe. ZnTe shares an edge with CdTe and therefore, can be considered chemically stable at the interface with CdTe.

The case of ZnTe/CdTe is a trivial scenario because of the presence of only two competing phases in the Cd-Zn-Te chemical space. Let us consider a more complex Cd-Te-O chemical space (ternary space for easier visualization) that has multiple competing phases. Figure 4(b) shows the 3D convex hull with CdTe sharing edges with rocksalt CdO (between chemical potentials marked by 1 and 2) and with $CdTeO_3$ (between 2 and 3). In contrast, the other phases in this ternary chemical space such as TeO_2 or Cd_3TeO_6 do not share an edge with CdTe and are likely to be chemically unstable at an interface with CdTe under thermodynamic equilibrium.

Among the 229 TBSs, we found 69 structures that exhibit bulk stability as well as interfacial chemical stability with CdTe. Among the 69 TBSs are 35 binary and 34 ternary compounds, including ZnTe as a benchmark material. Further analyses, including prediction of transport properties, band alignment, and p-type dopability focus on these 69 materials.

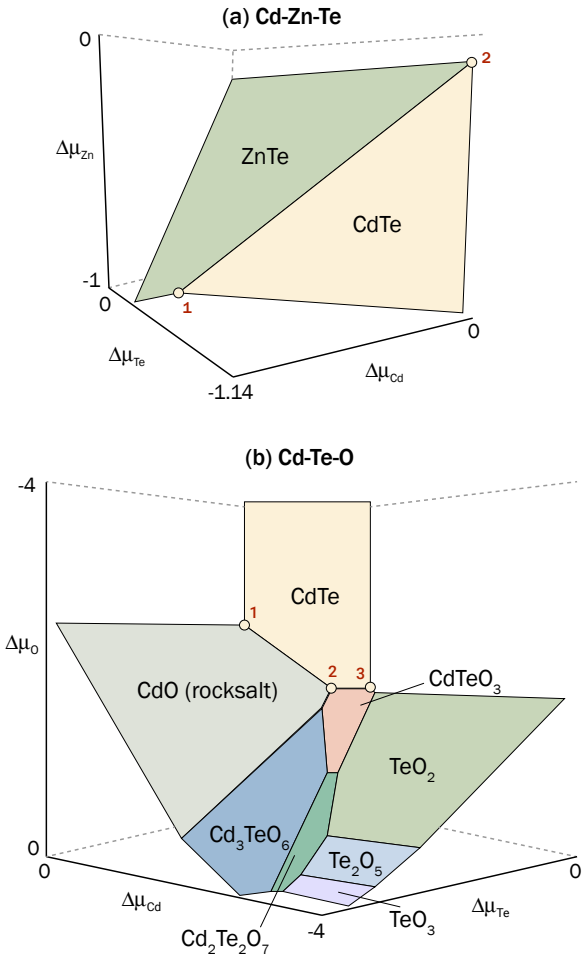

Figure 4: Visualization of the ternary convex hull in chemical potential space. $\Delta\mu_i$ is the deviation of the chemical potential of element i from the reference (standard) state. See section 6.5 for details. (a) In the Cd-Zn-Te chemical space, CdTe and ZnTe share an edge indicating interfacial chemical stability between the compounds. (b) In the Cd-Te-O chemical space, the interface between CdTe and rocksalt CdO is chemically stable in a limited range of chemical potentials bounded by 1 and 2. Similarly, CdTe/$CdTeO_3$ interface is stable between chemical potentials bounded by 2 and 3.

3.3. Electronic Structure and Transport Properties

The performance of the back contact is sensitive to its electronic structure and carrier transport properties. A suitable back contact for CdTe should ideally have a valence band alignment of no more than a few hundred meV relative to the valence band maximum (VBM) of CdTe. At the same time, the conduction band minimum (CBM) of the contact should be higher than the CBM of CdTe to enable electron reflection (Figure 1). Given these criteria and the fact that CdTe band gap is 1.50 eV, we conclude that the contact material should ideally have a band gap $E_g >$ 1.5 eV. For reference, E_g of ZnTe is 2.24 eV.[23] High hole mobility (μ_h), typically larger than 5-10 cm^2/Vs is desired for p-type back contacts to ensure good carrier transport. To this end, we calculated E_g and estimated μ_h (see Methods) of the 69 TBSs (Section 3.2) using DFT calculations.

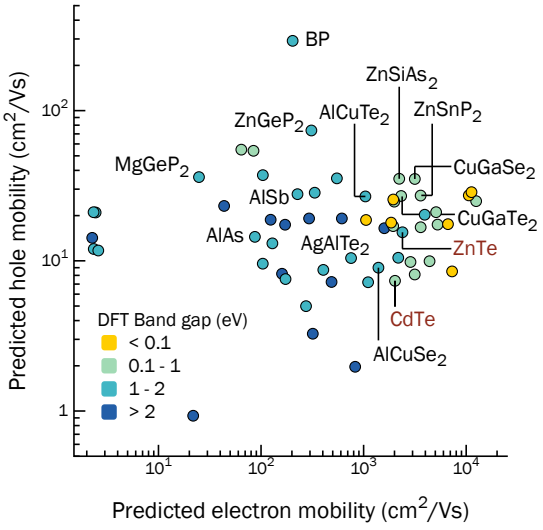

Figure 5: Predicted room-temperature hole and electron mobility of 58 tetrahedrally-bonded structures that fulfill the thermodynamic bulk and interfacial chemical stability criteria. Predicted carrier mobilities of CdTe are added for reference. The carrier mobilities were estimated with a semi-empirical model described in section 6.3. The color map indicates the band gap computed with density functional theory (DFT).

The underestimation of band gap with DFT is well known.[24] For example, E_g of CdTe and ZnTe calculated with DFT GGA functional are 0.60 and 1.07 eV, respectively. Because the underestimation is unsystematic, we adopted a conservative approach in screening potential materials based on their band gaps. Namely, we excluded TBSs with zero DFT E_g (11/69) from further consideration. After applying the minimum E_g criterion, we were left with 58 potential TBS candidates.

Next, we estimated the intrinsic, room-temperature hole (μ_h) and electron (μ_e) mobility in these 58 potential candidate materials using a semi-empirical model[25], where the input parameters such as bulk modulus (B) and band effective masses (m_b^*) are obtained from DFT calculations (see section 6.3 for details). The predicted μ_h and μ_e of the 58 TBSs are plotted in Figure 5, with the markers colored by their DFT band gap values. The mobility computed with the semi-empirical model provides an estimate of the intrinsic phonon scattering-limited mobility, and as such, should be treated as the upper limit. Additional sources of scattering such as ionized impurities in heavily-doped semiconductors will reduce the carrier mobility.[26] The computed properties of these 58 TBSs, including CdTe and ZnTe, are listed in Table S2.

As is generally found in semiconductors, μ_e tend to be larger than μ_h, mainly due to smaller conduction band effective masses. The predicted mobilities in Figure 5 are consistent with this trend, with the notable exception of BP, which has equally large electron and hole mobilities.[27] BP has recently been the subject of several computational and experimental studies as a potential p-type, non-oxide transparent conductor.[27, 28, 29] Some of the materials with high hole mobility (> 10 cm^2/Vs) and large DFT band gaps (> 1 eV) are labelled in Figure 5. II-IV-V_2 (e.g., $ZnSnP_2$) and I-III-VI_2 (e.g., $AlCuTe_2$) compounds feature prominently among them, in addition to Al-containing III-V compounds (e.g., AlSb).

Of the 51 TBSs shown in Figure 5, 48 are predicted to have $\mu_h > 5$ cm^2/Vs and 37 with $\mu_h > 10$ cm^2/Vs. The next steps in the downselection of the candidate materials involved determining the band alignment with CdTe and assessing p-type dopability. The band alignment and the dopability of a material are both sensitive to the band gap and therefore, DFT band gaps are unreliable for these purposes. We used the GW approximation to compute more accurate band gaps and individual band edge shifts (see section 6.3 for details). However, GW calculations are computationally resource intensive, which allowed us to consider only a subset of the 51 TBSs for further consideration.

We computed the GW band gap of 23 TBSs (including ZnTe), which were chosen by prioritizing materials that do not have either large ($E_g > 2.5$ eV) or small ($E_g < 0.5$ eV) DFT band gaps. The former are expected to be ultra-wide gap insulators, which are extremely challenging to dope,[30] and the latter are unlikely to have band gaps larger than CdTe (1.5 eV) and comparable to ZnTe (2.24 eV). The computed GW band gaps of the 23 TBSs are listed in Table S3. Where available, the experimental band gaps are also reported in Table S3. The GW band

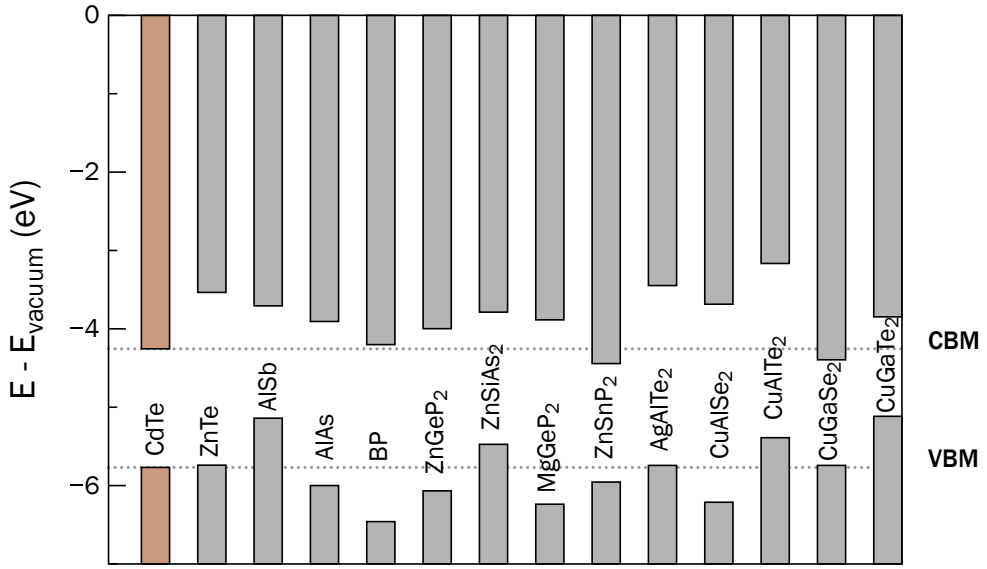

Figure 6: Computed conduction band (CB) and valence band (VB) alignments of 13 tetrahedrally-bonded structures relative to CdTe. ZnTe serves as a reference benchmark. The underestimation of the band gap in DFT was corrected by applying band edge shifts obtained from GW quasi-particle energy calculations (section 6.4). AlSb, $ZnSiAs_2$, $AgAlTe_2$, $CuAlTe_2$, and $CuGaTe_2$ satisfy the minimum criteria that the CB and VB are both higher than CdTe, which will enable electron reflection and hole transport at the interface with CdTe.

gaps of CdTe and ZnTe are 1.51 eV and 2.21 eV, respectively, which are in excellent agreement with their measured band gaps. Furthermore, we notice in Table S3 that the band gaps predicted with GW are generally in fair agreement with experimental measurements. The methodology adopted in our work has been shown to produce quantitative predictions of the ionization potentials and electron affinities of materials[31] as well as doping tendencies.[32, 33]

At this stage, we enlisted several guidelines based on heuristics (e.g, GW $E_g > 4$ eV, ultra wide band gap insulators) and practical fabrication-related challenges (e.g., need for high-temperature processing, ion mobility, previous experimental attempts) in conjunction with the computed electronic and transport properties to perform a further downselection to 13 candidate materials, including ZnTe.

3.4. Band Alignment and Lattice Matching with CdTe

A favorable band alignment between CdTe and the back contact is an important materials design criterion, as discussed in Section 2. To reiterate, specifically there are two primary requirements: (1) the CBM of the contact material should be at a higher energy than that of CdTe to facilitate electron reflection, and (2) the valence band alignment (Δ_{VB}) should ideally be within -0.4 eV to +0.3 eV to facilitate hole transport (barrier-less or small barrier for hole injection) and minimize efficiency losses (Figure 2). Band alignment is not an intrinsic property of a material pair, but instead depends on the specific details of the surface terminations, and whether interfacial defects are present that may pin the Fermi energy.[34] Nevertheless, for the purposes of materials evaluation, we computed the band alignment of the 13 candidate TBSs by invoking some physically-motivated assumptions. Here, band alignment is evaluated individually for each material rel-

ative to the vacuum (reference energy), using their DFT-relaxed structures. Determing real band offsets is complex and require accurate interface modeling, which is computationally intensive and must be considered on a case-by-case basis.

It is well-known that the (110) surface is the simplest non-polar termination of zinc blende structures.[35] The (110) surface is also the common non-polar termination of ternary chalcopyrites. Given the non-polar nature, large-scale surface reconstructions are not expected to occur, unlike on polar surfaces.[35, 36] Therefore, we uniformly computed the band alignment between the (110) surfaces of CdTe and the 13 candidate TBSs by referencing their VBM and CBM to the vacuum energy (see section 6.4 for details). The computed band alignments are summarized in Figure 6. Here, we assume that the band alignment calculated from the individual band edge positions reflects the band alignment at a real interface. Of course, interfacial defects and reconstructions induced by lattice mismatch will affect the actual band alignment, but these estimates are still a useful starting point to identify promising candidate materials.

We calculated the ionization potential of CdTe to be -5.8 eV, which is in good agreement with the measured value of 5.8-5.9 eV.[8, 15] Five out of the 13 TBSs exhibit the desired band edge positions i.e., -0.4 eV $\leq \Delta_{VB} \leq$+0.3 eV and CBM higher in energy than CdTe. In addition to ZnTe, we find AlAs, $ZnSiAs_2$, $ZnGeP_2$, and $AgAlTe_2$ posses these band edge feature. In addition, there are "sister structures" that may be alloyed to realize the desired band edge features and a means to tune lattice matching with CdTe. These include AlAs/AlSb, $CuAlSe_2$/$CuAlTe_2$, and $CuGaSe_2$/$CuGaTe_2$.

ZnTe: The band alignment of ZnTe/CdTe was calculated as a reference benchmark because ZnTe is widely used as the *p*-doped back contact in CdTe thin-film solar cells. Our calculations suggest that ZnTe has a near-ideal band alignment with a small positive VB alignment Δ_{VB} = 0.03 eV and significantly higher CB (Figure 6) owing to its large band gap of 2.2 eV. Our calculated band alignment is in agreement with similar calculations reported in the literature.[37, 38] We also simulated the interface band bending with SCAPS[22] using similar assumptions as in Section 2. Namely, we assumed *p*-type CdTe with hole doping of 10^{15} cm^{-3}, back contact hole doping of 10^{18} cm^{-3}, and for simplification, the same density of states for both the absorber and the back contact. In Figure 7(a), we find that the band bending is favorable for barrier-less hole transport from CdTe into ZnTe and simultaneously, electron reflection. However, there is a large lattice mismatch between the (110) planes of ZnTe and CdTe. Based on DFT-relaxed structures, we predict a 6.5% lattice mismatch, with CdTe possessing the larger lattice constant. Such a large lattice mismatch may lead to several outcomes, including highly strained (tensile) ZnTe near the interface, formation of dislocations, and other interface defects.[39, 40] As such, the near-ideal band alignment may be compromised when forming a real ZnTe/CdTe interface leading to low electron selectivity and high carrier recombination, as evident in experimental measurements.

AlAs, AlSb: These III-V compounds are interesting candidates because they are generally not as popular for functional applications as their well-known counterparts AlN, GaN, GaAs etc. The VBM of AlAs is 0.23 eV below that of CdTe (Figure 6), which is within the tolerable range of valence band alignment Δ_{VB} (Section 2). The simulated band bending, shown in Figure 7(b), indicates a small barrier for hole injection into AlAs. The band bending at the CB is similar to ZnTe, which is desired for electron reflection. However, AlAs has a very large lattice mismatch of 13.4% with CdTe in the (110) plane. The sister structure, AlSb, has a VBM that is 0.63 eV above CdTe; such a large positive Δ_{VB} is outside the tolerable range of valence band alignments. The simulated band bending, shown in Figure 7(c), exhibits a large barrier for hole injection. The downward sloping conduction band of CdTe will result in an electron sink at the interface causing significant carrier recombination. AlSb is slightly better lattice matched (5.9%) in the (110) plane, compared to ZnTe. Due to the smaller lattice constant, AlSb is also expected to be under tensile strain at the interface with CdTe. AlAs and AlSb

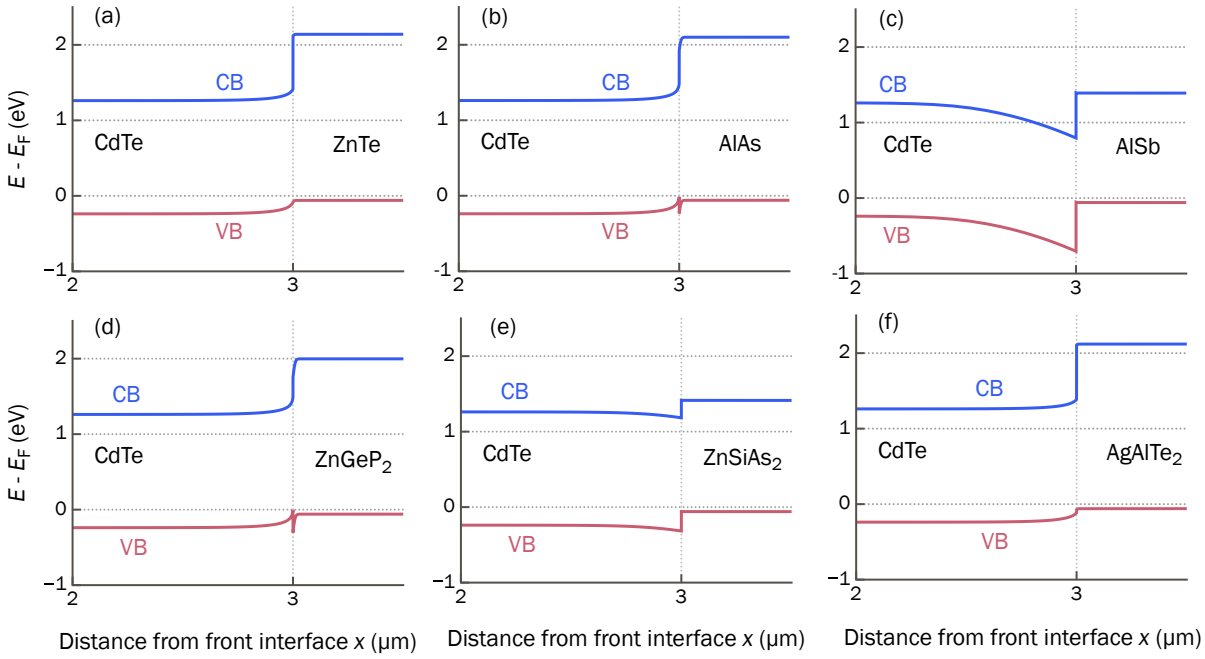

Figure 7: Band bending simulated with SCAPS[22] assuming p-type CdTe with hole concentration of 10^{15} cm^{-3}, back contact hole doping of 10^{18} cm^{-3}, and for simplification, the same density of states for both the absorber and the back contact. Band bending at the CdTe interface with (a) ZnTe, (b) AlAs, (c) AlSb, (d) $ZnGeP_2$, (e) $ZnSiAs_2$, and (f) $AgAlTe_2$, using the band alignments shown in Figure 6.

form a complete solid solution.[41, 42] Therefore, it may be possible to improve the lattice matching of AlAs by alloying with AlSb in way that also avoids the unfavorable band bending associated with AlSb.

$ZnSiAs_2$, $ZnGeP_2$: II-IV-V_2 compounds have been intensely studied as earth-abundant solar absorbers.[43] The VBM of $ZnSiAs_2$ and $ZnGeP_2$ are 0.3 eV above and -0.3 eV below CdTe, respectively, which is within the desired range of Δ_{VB}. Figures 7(d) and 7(e) are the simulated band bending at the interface with CdTe, which suggest that these II-IV-V_2 compounds are promising candidates with small barrier for hole injection. The CB bending in $ZnSiAs_2$ might result in electron accumulation at the interface; however, this effect will be limited because the depth of the potential well is relatively shallow.. In the (110) plane, the relevant lattice constants are a and b, which are equal for tetragonal $ZnSiAs_2$ (a = 5.68 Å) and $ZnGeP_2$ (a = 5.50 Å). Unlike zincblende ZnTe, AlAs, and AlSb, it is not immediately obvious how the lattices of these II-IV-V_2 compounds will match CdTe (6.62 Å). However, the large mismatch in the a, b lattice constants ($ZnSiAs_2$ – 14.2%, $ZnGeP_2$ – 16.9%) implies that the ZnSiAs2/CdTe interface may have a high concentration of dislocations or the interface may even turn amorphous.

$AgAlTe_2$: In our search, $AgAlTe_2$ has emerged as the most promising candidate material. Recent studies of $AgAlTe_2$ has focused on its application as an intermediate-band solar cell absorber,[44] but, to the best of our knowledge, has not been investigated as a back contact for CdTe solar cells. We predict that the band alignment of $AgAlTe_2$ is similar

to ZnTe, with a near-ideal VBM position with Δ_{VB} = +0.03 eV (Figure 6). The CBM position is also comparable to ZnTe owing to the similar band gaps (2.28 eV vs. 2.21 for ZnTe). Therefore, the simulated band bending for CdTe/$AgAlTe_2$ is almost identical to ZnTe. In addition to the favorable band alignment, the most attractive aspect of $AgAlTe_2$ is the smaller lattice mismatch (2.4%) with CdTe in the (110) plane, which may facilitate formation of less defective interfaces with CdTe.

$CuAlTe_2$, $CuAlSe_2$: I-III-VI_2 chalcopyrites have been researched as solar absorbers for more than three decades.[45, 46] We predict that Δ_{VB} of $CuAlTe_2$ and $CuAlSe_2$ are +0.38 eV and -0.44 eV, which are outside the tolerable range of VB alignments. $CuAlTe_2$ and $CuAlSe_2$ are known to form a complete solid solution. Since the Δ_{VB} of $CuAlTe_2$ and $CuAlSe_2$ are opposite in sign, one could optimize Δ_{VB} through alloying. $CuAlTe_2$ and $CuAlSe_2$ are, in fact, known to form a complete solid solution. In this case, while the band alignment could be tuned through alloying, the bigger challenge lies in the large lattice mismatches of 7.7% ($CuAlTe_2$) and 14.4% ($CuAlSe_2$) in the (110) plane. Perhaps, one could also envision alloying $CuAlTe_2$ with $AgAlTe_2$ to improve the *p*-type dopability of $AgAlTe_2$ (see Section 4).

$CuGaTe_2$, $CuGaSe_2$: These I-III-V_2 chalcopyrites are chemical analogues of $CuAlTe_2$ and $CuAlSe_2$, so it is not surprising to find that the band alignments show similar trends. The Δ_{VB} of $CuGaTe_2$ and $CuGaSe_2$ are +0.65 eV and +0.026 eV, respectively. On the other hand, the CBM of $CuGaTe_2$($CuGaSe_2$) is above(below) of CdTe. While Δ_{VB} of $CuGaSe_2$ is similar to ZnTe and $AgAlTe_2$, the lower CB is not desired because it will allow electron injection (rather than reflection) at the interface. The large lattice mismatch (>7% for $CuGaTe_2$, >14% for $CuGaSe_2$) remains an outstanding issue with this family of chalcopyrites as well. As noted above, it may be possible to form alloys among the different chalcopyrites because they are known to readily form solid solutions.[15]

In summary, we have identified AlAs and $AgAlTe_2$ as candidate TBSs based on their favorable valence band alignments. We have also considered their lattice matching with the (110) plane of CdTe and found that $AgAlTe_2$ may offer better lattice matching than ZnTe, which in turn might reduce interfacial defects and suppress deletrious carrier recombination. Finally, we have discussed the possibility of alloying between sister structures (AlAs/AlSb, $CuAlTe_2$/$CuAlSe_2$, $CuGaTe_2$/$CuGaSe_2$) as a means to fine tune the VB alignments and lattice matching.

3.5. p-type Dopability

The TBSs have to be doped *p*-type to be used as a hole-transporting back contact for CdTe solar cells. It is recommmended that the back contact should be at least moderately *p*-type with free hole concentration >10^{17}-10^{18} cm^{-3} so that an appreciable hole conductivity is achieved. Whether a material can be doped *p*-type (or *n*-type) fundamentally depends on the formation thermodynamics of the native defects. We used first-principles defect calculations to assess the *p*-type dopability of the candidate TBSs (see section 6.5 for details). Here, *p*-type dopability refers to the potential of a material to be doped *p*-type.

A material is considered *p*-type dopable if the most favorable native donor defect has high formation energy. In such a case, holes generated by a sufficiently soluble acceptor dopant are not compensated by the electrons created by the native donor. In other words, a "killer" donor defect is absent under the chosen conditions.[30] Accordingly, a *p*-type dopability window (ΔE_p) may be defined as a donor formation energy at the VBM, where a large positive ΔE_p indicates a highly *p*-type dopable material while a large negative window would suggest difficulty in *p*-type doping.

ZnTe can be doped *p*-type with Cu,[47] N,[48] or Sb[49] to achieve high hole concentrations in excess of 10^{19} cm^{-3}. We used first-principles defect calculations to assess the *p*-type dopability of AlAs, $AgAlTe_2$, and $CuAlTe_2$, which were identified as promising canidadates based on their stability, hole mobility, and band alignment with CdTe.

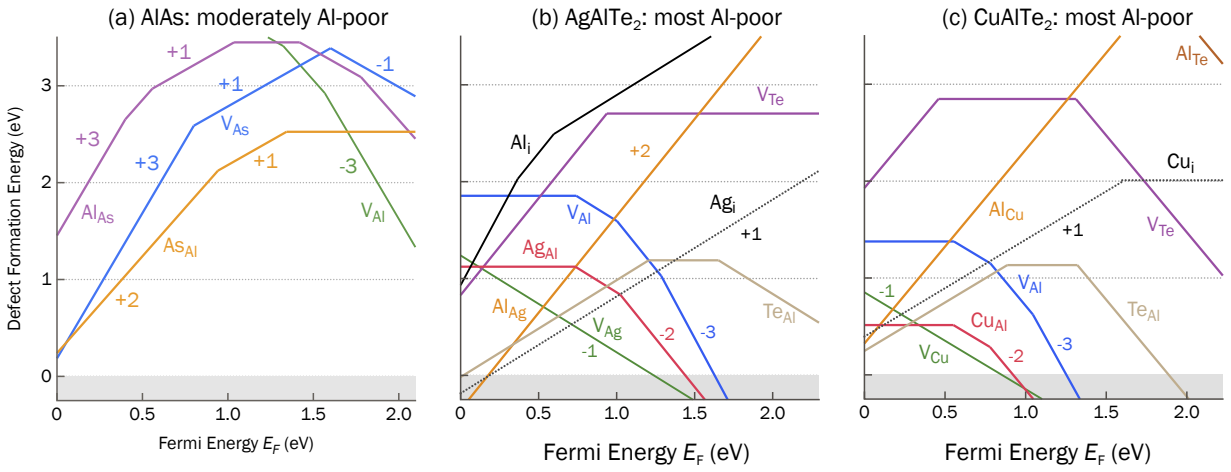

Figure 8: Formation energy ($\Delta E_{D,q}$) of native defects as a function of the Fermi energy (E_F) for (a) AlAs, under moderately Al-poor conditions, (b) $AgAlTe_2$, under the most Al-poor conditions, and (c) $CuGaTe_2$, under the most Al-poor conditions. The charge state (q) of certain defects are labelled next to the defect lines. The p-type dopability window (ΔE_p) is a measure of the likelihood that a material can be doped p-type. A large positive ΔE_p indicates a highly p-type dopable material while a large negative window would suggest difficulty in p-type doping.

AlAs: Our defect calculations suggest that AlAs is p-type dopable material with the largest ΔE_p of $\sim$0.2 eV under moderately Al-poor/As-rich conditions (Figure 8a). The lowest-energy donor (at Fermi energies closer to the valence band) changes between As vacancy (V_{As}), and anti-site defects (As_{Al}, Al_{As}) depending on the thermodynamic state determined by the Al and As chemical potentials. Al vacancy (V_{Al}) is the lowest energy acceptor (at Fermi energies closer to the conduction band) under most thermodynamic conditions. Due to the counterbalancing effect of chemical potentials on the different donor defects, the largest ΔE_p is obtained at moderately Al-poor/As-rich conditions, as opposed to under highly Al-rich/As-poor or Al-poor/As-rich conditions. The positive ΔE_p suggests that AlAs is p-type dopable. Our findings are consistent with several studies where p-type AlAs has been realized through group 14 doping (Si, C)[50, 51]; hole concentrations $> 10^{17}$ cm^{-3} have been reported. We also find that the formation energy of Al interstitials is very high. Therefore, unlike Cu, we do not expect Al interstitial diffusion to the interface or into CdTe to be an issue for p-type AlSb. However, diffusion of the p-type dopants (Si, C) as interstitials is still possible and requires careful consideration in selecting the dopants. We also know from experimental literature that AlSb can be doped p-type with hole concentrations as high as 10^{19} cm^{-3} with Mg, Be, and Si doping.[52, 53] In fact, carbon contamination during growth is known to be a cause for unintentional p-type doping of AlSb.[54]

$AgAlTe_2$: Among the different growth conditions, which are set by the elemental chemical potentials within the phase stability of $AgAlTe_2$, we find that the Al-poor growth conditions represents the best case scenario for p-type doping (Figure 8b). There are several low-energy native donors such as Ag interstitial (Ag_i), Al_{Ag} and Te_{Al} anti-site defects that limit p-type doping of $AgAlTe_2$. The p-type dopability window is -0.35 eV, which suggests that $AgAlTe_2$ can only be moderately doped p-type. While we have not performed an exhaustive search of possible p-type dopants, using realistic assumptions about the extrinsic acceptor dopant, we find that it is possible to achieve $> 10^{17}$ cm^{-3} hole concentrations (Figure SX in the supplementary information). We

have not found any experimental studies that have attempted p-type doping of $AgAlTe_2$. The low formation energy of Ag interstitials is another aspect of this material to contend with. Ag is known to diffuse into CdTe, introducing an acceptor level around 100 meV above the valence band maximum, and cause p-type doping of CdTe with hole concentrations in the 10^{16} cm^{-3} range.[55] This behavior is akin to Cu, which has its advantages and disadvantages.

$CuAlTe_2$: $CuAlTe_2$ is a known p-type chalcopyrite that has been grown in thin film form by RF sputtering[56] and is found to form a good ohmic contact with Mo, which has been used as the final back contact for CdTe. As-deposited $CuAlTe_2$ thin films are self-doped p-type. We confirm through our defect calculations that $CuAlTe_2$ is natively p-type under the most Al-poor growth conditions (Figure 8c) within the region of phase stability. The native p-type doping is due to the low formation energy of acceptor Cu vacancies (V_{Cu}) and Cu_{Al} anti-sites. Cu interstitials (Cu_i) and Te_{Al} are the lowest-energy native donors that limit the p-type dopability window (ΔE_p) to +0.25 eV. Under the most Cu-poor conditions, p-type dopability is limited by Al_{Cu} anti-site defects such that ΔE_p is -0.23 eV. As with other Cu-containing, electron-reflecting back contacts such as Cu_2Te and Cu-doped ZnTe, Cu is likely to diffuse from $CuAlTe_2$ into CdTe, which will facilitate p-type doping of CdTe but also cause long-term degradation issues.

We also know from existing experimental literature that $ZnSiAs_2$,[57] $ZnGeP_2$,[58] $CuAlSe_2$, and $CuGaSe_2$[15] are either natively p-type or can be extrinsically doped.

4. Discussion

Materials Recommendations and Challenges

We performed a computational search among 229 tetrahedrally-bonded structures to identify materials as new candidates for electron-reflecting back contact layers in CdTe thin film solar cells. Below, we summarize the findings for resultant candidate materials and validate our predictions through comparison with available experimental data. We also identify the key materials challenges and discuss possible design strategies to address them.

AlAs, AlSb: Metal pnictides have been little used as back contacts for CdTe solar cells. AlAs is the only binary compound identified as a candidate material in our search. Our GW computed band gap of 2.09 eV is in fair agreement with the experimentally measured value of 2.12 eV (Table S3). High hole mobilities ~100 cm^2/Vs at 300 K have been reported in MBE-grown crystals.[59] Based on the DFT-relaxed structure, we predict a large lattice mismatch of 13.4% between the (110) planes of AlAs and CdTe, which is larger compared to ZnTe (6.5%). The VBM of AlAs is 0.23 eV below that of CdTe, which is within the tolerable range of VB alignments. Hole-doped AlAs has been experimentally realized[59], and our defect calculations confirm its high p-type dopability. The migration of Al interstitials to the interface or into CdTe is not expected to be an issue due to the low concentrations of Al interstitials in AlAs. It may be possible to alloy AlAs with AlSb or even with CdTe, to achieve the desired lattice matching. While the actual interfacial band offset is far more complex and depends on the presence of point and extended defects and formation of space charges, our results provide early indications of the materials challenges to be expected in AlAs. Nevertheless, AlAs has certainly emerged as a promising material candidate that warrants further investigation. More in-depth studies will benefit from the existing experimental and theoretical literature on this material.

$AgAlTe_2$: With a better lattice matching and VBM that is almost aligned with that of CdTe, chalcopyrite $AgAlTe_2$ is the most attractive candidate identified in our search. $AgAlTe_2$ has been studied as a potential intraband solar absorber, but there is limited experimental data on the transport properties and doping. The band gap of $AgAlTe_2$ is 2.3 eV,[60] in agreement with our GW calculated band gap of 2.3 eV (Table S3). However, we predict that $AgAlTe_2$ is not highly p-type dopable; with

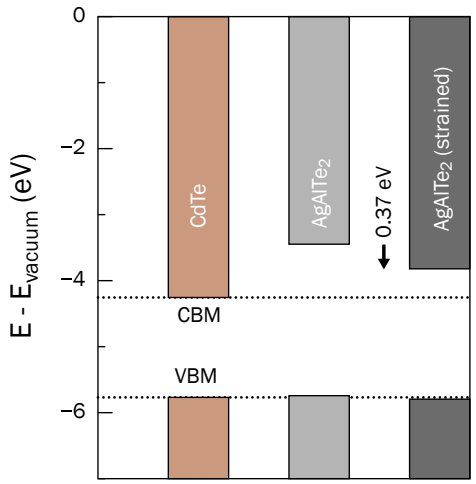

Figure 9: Effect of strain on the band alignment of $AgAlTe_2$. The lattice constants a and b are increased to match the lattice constant of CdTe. The underestimation of the band gap in DFT is corrected by applying band edge shifts obtained from GW quasi-particle energy calculations performed on the strained structures (section 6.4).

realistic assumptions, we predict that moderate hole concentrations on the order of 10^{17} cm^{-3} could be achieved through extrinsic doping. We also predict that Ag interstitials will be present in significant concentrations (Figure 8b). The presence of Ag interstitials in an analogous chalcopyrite, $AgInSe_2$, has been experimentally confirmed.[61] Ag diffusion into CdTe has the same effect as Cu i.e., it acts as p-type dopant, which is beneficial to achieve p-type CdTe but may contribute to long-term degradation similar to Cu. However, Ag^+ ions (1.0 Å, tetrahedral coordination) are much larger than Cu^+ (0.6 Å, tetrahedral coordination) and therefore, we can expect either reduced or sluggish migration of Ag^+ ions. As in the case of AlSb, we also simulated the effect of lattice strain on the band alignment of $AgAlTe_2$. We find that the CBM is lowered by 0.37 eV such that it is still higher than CdTe CBM (Figure 9b). The VBM remains almost unchanged and is aligned with the CdTe VBM. Overall, $AgAlTe_2$ is an attractive candidate that deserves further experimental development, in particular to address the p-type doping either through non-equilibrium doping in thin films or by alloying with other chalcopyrites discussed below. Chalcopyrites are highly amenable to alloying as evidenced by the numerous experimental studies.

$CuAlTe_2$, $CuAlSe_2$: The family of $CuAlCh_2$ (Ch = S, Se, Te) chalcopyrites has been extensively studied for multiple applications, including solar absorbers. We calculated the band gaps of $CuAlTe_2$ and $CuAlSe_2$ to be 2.2 eV and 2.5 eV, respectively, which are in fair agreement with experimental measurements (Table S3).[62] Hole mobilities of 5-6 cm^2/Vs and 18 cm^2/Vs have been reported for $CuAlTe_2$ and $CuAlSe_2$, respectively. p-type thin films of $CuAlTe_2$ and $CuAlSe_2$ have been grown, with hole concentrations $> 10^{21}$ cm^{-3} in $CuAlSe_2$. We confirmed with defect calculations that $CuAlTe_2$ is indeed highly p-type dopable. Due to the low formation energy of Cu interstitials (Figure 8c), Cu migration is expected along with the same advantages and disadvantages as Cu-doped ZnTe. The VBM of $CuAlTe_2$ is higher than CdTe by 0.4 eV, which could be tuned by alloying with $CuAlSe_2$; however, this may lead to an even larger lattice mistmatch with CdTe. Given the propensity of chalcopyrites to form alloys, it will be practical to consider alloys with $CuGaSe_2$, which has larger lattice constants than $CuAlSe_2$.

$CuGaTe_2$, $CuGaSe_2$: Like $CuAlCh_2$, $CuGaCh_2$ chalcopyrites have also been investigated as photovoltaic absorbers and for thermoelectrics.[63] $CuGaTe_2$ has a smaller band gap (1.24 eV) compared to $CuAlTe_2$. Our calculated band gap (1.26 eV) is in excellent agreement with experiments.[64] Furthermore, room-temperature hole mobilities in the range of 30-50 cm^2/Vs have been reported,[65, 66] which is within a factor of 2 of our predicted value (27 cm^2/Vs). Undoped $CuGaTe_2$ is natively p-type and hole concentrations on the order of 10^{18}-10^{19} cm−3 has been experimentally achieved through Ni, Mn, and Fe doping.[67, 65, 66] While the high hole mobility and p-type dopability are beneficial, the VB alignment relative to CdTe is large (Figure 6). It may be possible to control the VB alignment by alloying with

$CuGaSe_2$, but with a large lattice mistmatch ($> 7\%$ for $CuGaTe_2$) alloying with $CuGaSe_2$ will further reduce the lattice constants a and b, and increase the mistmatch with CdTe.

5. Conclusions

We performed a computational search among 229 binary and ternary tetrahedrally-bonded structures to identify new p-type back contacts to CdTe solar cells. Through device simulations, we established that valence band alignments $|\Delta_{VB}| \leq 0.3$ eV are desired to minimize reduction in efficiency. In addition to the band alignment criterion, we also considered interfacial chemical stability, high hole mobility, and p-type dopability as additional factors in identifying the candidate materials. We propose AlAs, $AgAlTe_2$, $ZnGeP_2$, $ZnSiAs_2$, and $CuAlTe_2$ as new back contacts that warrant further theoretical and experimentals investigations. We also propose alloys of these candidate materials with other "sister" structures to achieve the desired band alignment and lattice matching. We hope these material recommendations will be attractive alternatives to the currently used back contact, ZnTe. We find that there is no silver bullet that simultaneously fulfills all the materials design criteria but $AgAlTe_2$ comes close to being one.

Acknowledgments

We thank James Sites from Colorado State University for insightful discussions. The work was funded by First Solar Inc. through the National Renewable Energy Laboratory's CRADA program. The research was performed using computational resources sponsored by the Department of Energy's Office of Energy Efficiency and Renewable Energy and located at the NREL. The views expressed in the article do not necessarily represent the views of the DOE or the U.S. Government.

Author Contributions

G.X., W.M., and V.S. conceived the research project; P.G. and V.S. designed and executed the project; P.G. and D.K. performed the calculations and modeling; P.G. and V.S. analyzed the results with feedback from D.K., S.G., G.X, and W.M.; all authors participated in preparing and editing the manuscript.

Declaration of Interests

S.G., D.K., G.X., and W.M. work at First Solar, which is a publicly traded company that manufactures CdTe solar panels and develops grid-connected photovoltaic power plants. Outside of this and the funding listed in the acknowledgments section, the authors declare no competing interests.

6. Experimental Procedures

The computational workflow employed to downselect the candidate materials is schematically presented in Figure 3. We performed the search among materials documented in the Inorganic Crystal Structure Database (ICSD). We started by first identifying ordered and stoichiometric binary and ternary compounds that have tetrahedrally-bonded structures. Next, we used the convex hull analysis to determine the bulk thermodynamic phase stability as well as the interfacial chemical stability with CdTe. We calculated the electronic structure and hole mobility for those structures that satisfy the thermodynamic stability criteria. Materials that were predicted to have a desired band gap and relatively high hole mobility were then asssessed for their band alignment relative to CdTe. Finally, we used first-principles calculations to evaluate the p-type dopability of the candidate structures with the desired band alignments.

6.1. Tetrahedrally-bonded Structures

We developed an automated procedure to identify tetrahedrally-bonded structures (TBSs). For a structure to qualify as a TBS, we used the following two criteria: (1) each atom in the structure

should have four nearest neighbors, and (2) the angle formed by the three atoms - the central atom and two atoms at adjacent vertices of the tetrahedron, is 109.5±10°. We allowed a tolerance of ±10° from the ideal tetrahedral angle (109.5°) to accommodate otherwise TBSs with small distortions. The nearest neighbor search and calculation of the angles was performed with the Pylada framework, which is a Python-based software package for automation of high-throughput density functional theory (DFT) calculations and contains modules for crystal structure analysis and manipulation.[68]

6.2. Thermodynamic Bulk and Interface Stability

We assessed the thermodynamic bulk and interface stability of TBSs from grand potential phase diagrams obtained through convex hull construction. Bulk stability implies that the TBS is thermodynamically stable against decomposition into competing phases. Similarly, interfacial stability implies that the TBS is chemically stable in contact with CdTe under some chemical potential conditions. See Section 3.2 for a more detailed discussion of bulk and interfacial stability.

We considered all competing phases that are documented in the ICSD in constructing the convex hull (in the chemical potential space). In most cases, the DFT total energies needed for the convex hull construction were taken from the NREL Materials Database.[69] For the remaining structures, we relaxed the ICSD structures with DFT using the plane-wave VASP code.[70] The Perdew-Burke-Ernzerhof (PBE) exchange correlation functional was used within the generalized gradient approximation (GGA).[71] The valence electrons were treated with the projector-augmented wave (PAW) method. The structures are relaxed with a plane-wave energy cutoff of 340 eV and a Monkhorst-Pack k-point sampling. The formation enthalpy of each TBS and competing phase was calculated from their DFT total energy and reference chemical potentials of the elemental phases. We used the fitted elemental-phase reference energies (FERE) as the reference chemical potentials, which has been shown to provide accurate predictions of formation enthalpy.[72]

6.3. Electronic Structure and Carrier Mobility

The DFT electronic structures were calculated on the relaxed structures using the GGA-PBE functional. Electronic structures were calculated on a dense k-mesh with a fixed number of k-points. The k-point grid was determined according to the equation: $N_{\text{atoms}} \times N_{\text{kpts}} \simeq 8000$, where N_{atoms} is the number of atoms in the primitive cell and N_{kpts} is the number of k points. The room-temperature, intrinsic carrier mobility (μ) was estimated with a semi-empirical model[25] given by,

$$\mu = AB^s \left(m_b^*\right)^{-t} \tag{1}$$

where B is the bulk modulus, m_b^* the band effective mass, and A, s, and t are fitted constants. Bulk modulus B is obtained by fitting the Birch-Murnaghan equation of state to a set of DFT total energies computed at different fixed volumes around the equilibrium structure. The density-of-steates (DOS) effective mass (m^*_{DOS}) is determined from the DOS within the single parabolic band approximation, such that the parabolic band reproduces the same number of states as the DOS within a 100 meV energy window from the relevant band edges e.g., states between VBM and VBM - 0.1 eV. With m^*_{DOS} and band degeneracy (N_{b}), the band effective mass (m^*_{b}) can be determined within the parabolic and isotropic band approximation as $m^*_{\text{b}} = m^*_{\text{DOS}}\ N_{\text{b}}^{-2/3}$. We have demonstrated that the semi-empirical model predicts the room-temperature μ within half an order of magnitude of the measured values,[25] which itself exhibits orders of magnitude variations depending on the synthesis procedure and sample preparation. Therefore, the prediction accuracy of the model is acceptable for rapid screening of a large number of materials.[73, 74]

The underestimation of the band gap in DFT was corrected by applying individual valence and conduction band edge shifts (relative to the DFT-computed band edges) as determined from GW quasi-particle energies.[75] We used DFT-PBE wave functions as input to the GW calculations. The GW eigenvalues were then iterated to self-consistency removing the dependence of the single-particle energies on the initial DFT calculation. The input DFT wave functions were kept constant during the GW calculations,

which allows the interpretation of the GW quasiparticle energies in terms of energy shifts relative to the Kohn-Sham energies. The GW band edge shifts were utilized to correct the band alignment and band gap in the defect calculations.

6.4. Band Alignment

The band alignments were computed using the standard slab supercell approach, wherein the energy is referenced to the vacuum energy.[31, 76, 77, 78] Slab supercells with (110) non-polar surface terminations were constructed from the bulk crystal structures that were previously relaxed with DFT-PBE functional (Section 6.2). The slabs containing 8-12 "layers" of atoms were separted by 10 Å of vacuum to prevent spurious interaction between the periodic images of the slabs. The atomic positions in the slab supercells were relaxed with DFT-PBE functional until the residual forces on the atoms were below 0.01 eV/Å. The thickness of the slabs was tested for convergence of the band alignment; with the chosen slab thickness, the spatially-averaged (in the direction of the vacuum) electrostatic potential in the center of the slab was flat and did not exhibit perturbations due to the surface effects. In other words, the centers of the slabs reproduced the bulk behavior. Finally, the VBM and CBM positions were corrected using the band edge shifts calculated from GW quasiparticle energy calculations (Section 6.3).

For $AgAlTe_2$, we calculated the band alignment of the strained structure. The lattice constants a and b were stretched to match the lattice constant of CdTe. To find the pseudo ground-state of the strained structures, we sketched the equation of state by calculating the total energy at different scaling of the c axis. We identified the c axis scaling that minimizes the energy and created slab supercells of the strained structure with elongated a and b and scaled c. The VBM and CBM positions were corrected with band edge shifts calculated from GW quasi-particle energy calculations on the scaled unit cell.

6.5. Defect Energetics

The defect energetics were calculated using the standard supercell approach,[79, 80] in which the defect formation energy is given by,

$$\Delta E_{D,q} = E_{D,q} - E_{\text{host}} + \sum_i n_i \mu_i + q E_{\text{F}} + E_{\text{corr}} \tag{2}$$

where $\Delta E_{D,q}$ is the formation energy of defect D in charge state q, E_{D^q} and E_{host} are the total energies of the supercell with and without the defect respectively, and E_{F} is the Fermi energy. The total energies were obtained with DFT-PBE functional by relaxing the atomic positions in the supercells. Supercells containing 216 atoms atoms were used to compute the defect energetics in AlAs, $AgAlTe_2$, and $CuAlTe_2$.

The chemical potential μ_i of element i is expressed relative to a reference state (μ_i^0) such that $\mu_i = \mu_i^0 + \Delta\mu_i$. A certain number of atoms (n_i) of element i are added ($n_i < 0$) or removed ($n_i > 0$) from the host supercell to form the defect D. The FERE chemical potentials (Section 6.2) were used as the reference chemical potentials of the elemental phases.[72] The bounds on $\Delta\mu_i$ are set by thermodynamic phase stability conditions, which are obtained through a convex hull analysis, as described in Section 6.2. In experiments, $\Delta\mu_i = 0$ corresponds to i-rich growth conditions and a large negative value of $\Delta\mu_i$ represents i-poor growth conditions.

Corrections to the defect formation energy arising from finite-size effects were included in E_{corr}, following the methodology of Lany and Zunger.[79, 81] The finite-size corrections include: (i) alignment of the average electrostatic potential between the neutral, defect-free host supercell and the charged, defected supercells, (ii) removal of artificial, long-range interactions between the image charges in periodic supercells that are charged, and (iii) correction for Moss-Burnstein-type band filling due to shallow defects. It is well-known that DFT underestimates the band gap of semiconductors, which can affect the calculated defect formation energies and charge carrier concentrations. We address the band gap issue by applying shifts to the band edge positions based on GW quasiparticle energy calculations,[75] described in Section 6.3. Formation energies of all point defects that contribute electrons to the conduction band or holes to the valence band are corrected by adding $q\Delta E_{CBM}$

for electrons or subtracting $q\Delta E_{VBM}$ for holes, respectively. Here, q denotes the number of electrons or holes and ΔE_{CBM} and ΔE_{VBM} are the individual band-edge shifts (relative to DFT) obtained from GW calculations.

The pylada-defects software package was used in this work for automating the point defect calculations, including the creation of defect supercells and calculation of finite-size corrections.[82] The formation energies of native point defects (vacancy, antisite, interstitial) were calculated in charge states q = -3, -2, -1, 0 , +1, +2, and +3. Additional charge states were considered where necessary. The plausible sites that can accommodate interstitial defects were determined by a Voronoi tessellation scheme implemented in pylada-defects.[82] The lowest-energy interstitial site was determined from the total energy of the interstitial configurations in the neutral charge state.

6.6. Band Bending and Device Efficiency

Equilibrium band structures i.e., band bending, was calculated using the SCAPS solver at 300K.[22] The model consists of 3 layers: CdTe absorber with p-doping of 10^{15} cm^{-3} (unless stated otherwise) and thickness of 3 μm, back contact layer with p-doping of 10^{18} cm^{-3} (unless stated otherwise) and thickness of 0.5 μm, and front SnO_2 layer with n-doping of 10^{20} cm^{-3} and thickness of 0.5 μm. The dielectric permittivity is set to 10, and the conduction and valence band density of states are set to 10^{19} cm^{-3} for both layers for simplicity. Boundary conditions for potential are set to "flat bands".

References

[1] NREL PV Chart. Best research-cell efficiency chart. www.nrel.gov/pv/cell-efficiency.html; Accessed July 2022.

[2] Metzger, W.K., Grover, S., Lu, D., Colegrove, E., Moseley, J., Perkins, C.L., et al. Exceeding 20% efficiency with in situ group v doping in polycrystalline CdTe solar cells. Nat Energy 2019;4(10):837. URL: dx.doi.org/10.1038/s41560-019-0446-7.

[3] Duenow, J.N., Metzger, W.K.. Back-surface recombination, electron reflectors, and paths to 28% efficiency for thin-film photovoltaics: A CdTe case study. J Appl Phys 2019;125(5):053101. URL: https://doi.org/10.1063/1.5063799.

[4] Krasikov, D., Sankin, I.. Defect interactions and the role of complexes in the CdTe solar cell absorber. J Mater Chem A 2017;5:3503–3513. URL: https://doi.org/10.1039/C6TA09155E.

[5] Krasikov, D.. Selenium lowers bulk recombination. Nature Energy 2019;4(6):442–443. doi:https://doi.org/10.1038/s41560-019-0393-3.

[6] Kuciauskas, D., Farrell, S., Dippo, P., Moseley, J., Moutinho, H., Li, J.V., et al. Charge-carrier transport and recombination in heteroepitaxial CdTe. J Appl Phys 2014;116(12):123108. URL: https://doi.org/10.1063/1.4896673.

[7] Kanevce, A., Reese, M.O., Barnes, T.M., Jensen, S.A., Metzger, W.K.. The roles of carrier concentration and interface, bulk, and grain-boundary recombination for 25% efficient CdTe solar cells. J Appl Phys 2017;121(21):214506. URL: https://doi.org/10.1063/1.4984320.

[8] Hall, R.S., Lamb, D., Irvine, S.J.C.. Back contacts materials used in thin film CdTe solar cells—a review. Energy Science & Engineering 2021;9:606–632. URL: https://doi.org/10.1002/ese3.843.

[9] McCandless, B.E., Sites, J.R.. Cadmium telluride solar cells. Handbook of photovoltaic science and engineering 2003;:617–662.

[10] Kumar, S.G., Rao, K.S.R.K.. Physics and chemistry of CdTe/CdS thin film heterojunction photovoltaic devices: fundamental and critical aspects. Energy Environ Sci 2014;7:45–102. URL: http://dx.doi.org/10.1039/C3EE41981A.

[11] Platzer-Björkman, C., Barreau, N., Bär, M., Choubrac, L., Grenet, L., Heo, J., et al.

Back and front contacts in kesterite solar cells: state-of-the-art and open questions. Journal of Physics: Energy 2019;1:044005. URL: https://doi.org/10.1088/2515-7655/ab3708.

[12] Reese, M.O., Perkins, C.L., Burst, J.M., Farrell, S., Barnes, T.M., Johnston, S.W., et al. Intrinsic surface passivation of CdTe. J Appl Phys 2015;118(15):155305. URL: https://doi.org/10.1063/1.4933186.

[13] Wu, X., Zhou, J., Duda, A., Yan, Y., Teeter, G., Asher, S., et al. Phase control of Cu_xTe film and its effects on CdSCdTe solar cell. Thin Solid Films 2007;515(15):5798–5803. URL: https://doi.org/10.1016/j.tsf.2006.12.151.

[14] Türck, J., Siol, S., Mayer, T., Klein, A., Jaegermann, W.. Cu_2S as ohmic back contact for CdTe solar cells. Thin Solid Films 2015;582:336–339. URL: https://doi.org/10.1016/j.tsf.2014.11.017.

[15] Woods-Robinson, R., Ablekim, T., Norman, A., Johnston, S., Persson, K.A., Reese, M.O., et al. Sputtered p-type $Cu_xZn_{1-x}S$ back contact to CdTe solar cells. ACS Applied Energy Materials 2020;3(6):5427–5438. URL: https://doi.org/10.1021/acsaem.0c00413.

[16] Guo, D., Brinkman, D., Shaik, A.R., Sankin, I., Krasikov, D., Ringhofer, C., et al. Modeling metastability in CdTe solar cells due to cu migration. In: Workshop on Coupled Mathematical Models for Physical and Nanoscale Systems and their Applications. Springer; 2016, p. 187–213.

[17] Krasikov, D., Knizhnik, A., Potapkin, B., Selezneva, S., Sommerer, T.. First-principles-based analysis of the influence of Cu on CdTe electronic properties. Thin Solid Films 2013;535:322–325. URL: https://doi.org/10.1016/j.tsf.2012.10.027.

[18] Kranz, L., Gretener, C., Perrenoud, J., Schmitt, R., Pianezzi, F., La Mattina, F., et al. Doping of polycrystalline CdTe for high-efficiency solar cells on flexible metal foil. Nature Communications 2013;4(1):1–7. URL: https://doi.org/10.1038/ncomms3306.

[19] Curtarolo, S., Hart, G.L., Nardelli, M.B., Mingo, N., Sanvito, S., Levy, O.. The high-throughput highway to computational materials design. Nature Materials 2013;12(3):191–201. URL: https://doi.org/10.1038/nmat3568.

[20] Gorai, P., Stevanović, V., Toberer, E.S.. Computationally guided discovery of thermoelectric materials. Nature Reviews Materials 2017;2:1–16. URL: https://doi.org/10.1038/natrevmats.2017.53.

[21] Belsky, A., Hellenbrandt, M., Karen, V.L., Luksch, P.. New developments in the inorganic crystal structure database (icsd): Accessibility in support of materials research and design. Acta Crystallogr B 2002;58:364. URL: https://doi.org/10.1107/S0108768102006948.

[22] Burgelman, M., Nollet, P., Degrave, S.. Modelling polycrystalline semiconductor solar cells. Thin Solid Films 2000;361-362:527–532. URL: https://doi.org/10.1016/S0040-6090(99)00825-1.

[23] Rao, G.K., Bangera, K.V., Shivakumar, G.. The effect of substrate temperature on the structural, optical and electrical properties of vacuum deposited ZnTe thin films. Vacuum 2009;83:1485–1488. URL: https://doi.org/10.1016/j.vacuum.2009.06.047.

[24] van Schilfgaarde, M., Kotani, T., Faleev, S.. Quasiparticle self-consistent *gw* theory. Phys Rev Lett 2006;96:226402. doi:https://doi.org/10.1103/PhysRevLett.96.226402.

[25] Yan, J., Gorai, P., Ortiz, B., Miller, S., Barnett, S.A., Mason, T., et al. Material descriptors for predicting thermoelectric performance. Energy Environ Sci 2015;8:983–994. URL: http://dx.doi.org/10.1039/C4EE03157A.

[26] Peter, Y., Cardona, M.. Fundamentals of semiconductors: physics and materials properties. Springer Science & Business Media; 2010.

[27] Ha, V.A., Karasulu, B., Maezono, R., Brunin, G., Varley, J.B., Rignanese, G.M., et al. Boron phosphide as a *p*-type transparent conductor: Optical absorption and transport through electron-phonon coupling. Phys Rev Materials 2020;4:065401. doi:https://doi.org/10.1103/PhysRevMaterials.4.065401.

[28] Willis, J., Scanlon, D.O.. Latest directions in p-type transparent conductor design. J Mater Chem C 2021;9:11995–12009. URL: http://dx.doi.org/10.1039/D1TC02547C.

[29] Crovetto, A., Adamczyk, J.M., Schnepf, R.R., Perkins, C.L., Hempel, H., Bauers, S.R., et al. Boron phosphide films by reactive sputtering: Searching for a p-type transparent conductor. arXiv preprint arXiv:211207474 2021;.

[30] Goyal, A., Gorai, P., Anand, S., Toberer, E.S., Snyder, G.J., Stevanovic, V.. On the dopability of semiconductors and governing material properties. Chemistry of Materials 2020;32:4467–4480. URL: https://doi.org/10.1021/acs.chemmater.9b05126.

[31] Stevanovic, V., Lany, S., Ginley, D.S., Tumas, W., Zunger, A.. Assessing capability of semiconductors to split water using ionization potentials and electron affinities only. Phys Chem Chem Phys 2014;16:3706–3714. URL: http://dx.doi.org/10.1039/C3CP54589J.

[32] Goyal, A., Gorai, P., Toberer, E.S., Stevanović, V.. First-principles calculation of intrinsic defect chemistry and self-doping in PbTe. npj Comput Mater 2017;3(1):1. URL: https://doi.org/10.1038/s41524-017-0047-6.

[33] Gorai, P., Ortiz, B.R., Toberer, E.S., Stevanović, V.. Investigation of n-type doping strategies for Mg_3Sb_2. J Mater Chem A 2018;6(28):13806. URL: https://doi.org/10.1039/C8TA03344G.

[34] Williams, R.H., Patterson, M.H.. Fermi level pinning at metal-CdTe interfaces. Applied Physics Letters 1982;40:484–486. URL: https://doi.org/10.1063/1.93151.

[35] Jaffe, J.E., Zunger, A.. Defect-induced nonpolar-to-polar transition at the surface of chalcopyrite semiconductors. Phys Rev B 2001;64:241304. URL: https://doi.org/10.1103/PhysRevB.64.241304.

[36] Gorai, P., Seebauer, E.G., Ertekin, E.. Mechanism and energetics of O and O_2 adsorption on polar and non-polar ZnO surfaces. The Journal of Chemical Physics 2016;144:184708. URL: https://doi.org/10.1063/1.4948939.

[37] Wei, S.H., Zunger, A.. Calculated natural band offsets of all II–VI and III–V semiconductors: Chemical trends and the role of cation d orbitals. Applied Physics Letters 1998;72(16):2011–2013. URL: https://doi.org/10.1063/1.121249.

[38] Van de Walle, C.G., Neugebauer, J.. Universal alignment of hydrogen levels in semiconductors, insulators and solutions. Nature 2003;423(6940):626–628. URL: https://doi.org/10.1038/nature01665.

[39] Cibert, J., Gobil, Y., Dang, L.S., Tatarenko, S., Feuillet, G., Jouneau, P.H., et al. Critical thickness in epitaxial CdTeZnTe. Applied Physics Letters 1990;56:292–294. URL: https://doi.org/10.1063/1.102812.

[40] Kret, S., Dluzewski, P., Dluzewski, P., Laval, J.Y.. On the measurement of dislocation core distributions in a GaAs/ZnTe/CdTe heterostructure by high-resolution transmission electron microscopy. Philosophical Magazine 2003;83:231–244. URL: https://doi.org/10.1080/0141861021000020095.

[41] Bolognesi, C., Werking, J., Caine, E., Kroemer, H., Hu, E.. Microwave performance of a digital alloy barrier Al(Sb,As)/AlSb/InAs heterostructure field-effect transistor. IEEE Electron Device Letters 1993;14:13–15. URL: https://doi.org/10.1109/55.215085.

[42] Al-Assiri, M.S., Bouarissa, N.. Electronic band structure and derived properties

of $AlAs_xSb_{1-x}$ alloys. Superlattices and Microstructures 2013;59:144–154. URL: https://doi.org/10.1016/j.spmi.2013.04.007.

[43] Martinez, A.D., Fioretti, A.N., Toberer, E.S., Tamboli, A.C.. Synthesis, structure, and optoelectronic properties of II–IV–V_2 materials. J Mater Chem A 2017;5:11418–11435. URL: https://doi.org/10.1039/C7TA00406K.

[44] Huang, D., Jiang, J.W., Guo, J., Zhao, Y.J., Chen, R., Persson, C.. Group-IV (Si, Ge, and Sn)-doped $AgAlTe_2$ for intermediate band solar cell from first-principles study. Semiconductor Science and Technology 2017;32(6):065007. URL: https://doi.org/10.1088/1361-6641/aa67d7.

[45] Pamplin, B.R., Kiyosawa, T., Masumoto, K.. Ternary chalcopyrite compounds. Progress in Crystal Growth and Characterization 1979;1:331–387. URL: https://doi.org/10.1016/0146-3535(79)90002-9.

[46] Siebentritt, S.. Wide gap chalcopyrites: material properties and solar cells. Thin Solid Films 2002;403-404:1–8. URL: https://doi.org/10.1016/S0040-6090(01)01525-5.

[47] Gessert, T., Mason, A., Reedy, R., Matson, R., Coutts, T., Sheldon, P.. Development of rf sputtered, Cu-doped ZnTe for use as a contact interface layer to p-CdTe. Journal of electronic materials 1995;24(10):1443–1449. URL: https://doi.org/10.1007/BF02655462.

[48] Spath, B., Fritsche, J., Klein, A., Jaegermann, W.. Nitrogen doping of ZnTe and its influence on CdTeZnTe interfaces. Applied Physics Letters 2007;90:062112. URL: https://doi.org/10.1063/1.2459589.

[49] Barati, A., Klein, A., Jaegermann, W.. Deposition and characterization of highly p-type antimony doped ZnTe thin films. Thin Solid Films 2009;517:2149–2152. URL: https://doi.org/10.1016/j.tsf.2008.10.078.

[50] Chand, N., Henderson, T., Klem, J., Masselink, W.T., Fischer, R., Chang, Y.C., et al. Comprehensive analysis of Si-doped $Al_xGa_{1-x}As$ ($x = 0 - -1$): Theory and experiments. Phys Rev B 1984;30:4481–4492. URL: https://doi.org/10.1103/PhysRevB.30.4481.

[51] Sekiguchi, S., Miyamoto, T., Kimura, T., Koyama, F., Iga, K.. Heavy p-type carbon doping to AlAs for InP based optoelectronic devices. In: 11th Annual Meeting. IEEE Lasers and Electro-Optics Society 1998; vol. 2. 1998, p. 126–127. URL: https://doi.org/10.1109/LEOS.1998.739493.

[52] Bennett, B.R., Moore, W.J., Yang, M.J., Shanabrook, B.V.. Transport properties of Be- and Si-doped AlSb. Journal of Applied Physics 2000;87:7876–7879. URL: https://doi.org/10.1063/1.373470.

[53] Shawon, A.A., Rahman, M.M., Ur, S.C.. Improvement of thermoelectric properties of AlSb by incorporation of mg as p-type dopant. Electronic Materials Letters 2020;16(6):540–547. URL: https://doi.org/10.1007/s13391-020-00241-0.

[54] McCluskey, M.D., Haller, E.E., Becla, P.. Carbon acceptors and carbon-hydrogen complexes in AlSb. Phys Rev B 2001;65:045201. URL: https://doi.org/10.1103/PhysRevB.65.045201.

[55] Chamonal, J., Molva, E., Pautrat, J., Revoil, L.. Complex behaviour of Ag in CdTe. Journal of Crystal Growth 1982;59:297–300. URL: https://doi.org/10.1016/0022-0248(82)90340-2.

[56] El Assali, K., Chahboun, N., Bekkay, T., Ameziane, E., Boustani, M., Khiara, A.. Electrical properties of $CuAlTe_2$ thin films and $MoCuAlTe_2$ contact prepared by rf sputtering. Solar Energy Materials and Solar Cells 1995;39:33–38. URL: https://doi.org/10.1016/0927-0248(95)00037-2.

[57] Koroleva, L.I., Zashchirinskii, D., Khapaeva, T., Marenkin, S., Fedorchenko, I., Szymczak, R., et al. Manganese-doped $ZnSiAs_2$ chalcopyrite: A new advanced material for spintronics. Physics of the Solid state 2009;51(2):303–308. URL: https://doi.org/10.1134/S1063783409020164.

[58] Somogyi, K., Bertóti, I.. Some electrical properties of $ZnGeP_2$ crystals. Japanese Journal of Applied Physics 1972;11:103–106. URL: https://doi.org/10.1143/jjap.11.103. doi:10.1143/jjap.11.103.

[59] Look, D.C., Lorance, D.K., Sizelove, J.R., Stutz, C.E., Evans, K.R., Whitson, D.W.. Alloy scattering in p-type $Al_xGa_{1-x}As$. J Appl Phys 1992;71:260–266. URL: https://doi.org/10.1063/1.350752.

[60] Uruno, A., Usui, A., Kobayashi, M.. Structural and optical properties of $AgAlTe_2$ layers grown on sapphire substrates by closed space sublimation method. J Appl Phys 2014;116:183504. URL: https://doi.org/10.1063/1.4901468.

[61] Krustok, J., Raudoja, J., Krunks, M., Mändar, H., Collan, H.. Nature of the native deep localized defect recombination centers in the chalcopyrite and orthorhombic $AgInS_2$. Journal of Applied Physics 2000;88:205–209. URL: https://doi.org/10.1063/1.373644.

[62] Gombia, E., Leccabue, F., Pelosi, C.. The cvd growth of $CuAlTe_2$ single crystals. Materials Letters 1984;2:429–431. URL: https://doi.org/10.1016/0167-577X(84)90155-1.

[63] Plirdpring, T., Kurosaki, K., Kosuga, A., Day, T., Firdosy, S., Ravi, V., et al. Chalcopyrite $CuGaTe_2$: A high-efficiency bulk thermoelectric material. Advanced Materials 2012;24:3622–3626. URL: https://doi.org/10.1002/adma.201200732.

[64] León, M., Díaz, R., Rueda, F., Berghol, M.. A comparative study of optical, electrical and structural properties of $CuGaSe_2$ and $CuGaTe_2$ thin films. Solar Energy Materials and Solar Cells 1992;26:295–307. URL: https://doi.org/10.1016/0927-0248(92)90049-U.

[65] Wasim, S., Marcano, G., Pérez, G.S.. Electrical properties of $CuGaTe_2$. physica status solidi (a) 1983;78:423–430. URL: https://doi.org/10.1002/pssa.2210780207.

[66] Šantić, B.. Electrical properties of $CuGa_xIn_{1-x}Te_2$ semiconductors. physica status solidi (a) 1992;133:137–146. URL: https://doi.org/10.1002/pssa.2211330114.

[67] Zhang, Z., Gao, Y., Wu, Y., Wang, B., Sun, W., Yu, L., et al. P-type doping of transition metal elements to optimize the thermoelectric properties of $CuGaTe_2$. Chemical Engineering Journal 2022;427:131807. URL: https://doi.org/10.1016/j.cej.2021.131807.

[68] Pylada:. Pylada: A python-based package for automation of first-principles calculations. github.com/pylada; ????

[69] NRELMatDB:. Nrel materials database. materials.nrel.gov; ????

[70] Kresse, G., Furthmüller, J.. Efficient iterative schemes for ab initio total-energy calculations using a plane-wave basis set. Phys Rev B 1996;54:11169–11186. URL: https://doi.org/10.1103/PhysRevB.54.11169.

[71] Perdew, J.P., Burke, K., Ernzerhof, M.. Generalized gradient approximation made simple. Phys Rev Lett 1996;77:3865–3868. doi:https://doi.org/10.1103/PhysRevLett.77.3865.

[72] Stevanovic, V., Lany, S., Zhang, X., Zunger, A.. Correcting density functional theory for accurate predictions of compound enthalpies of formation: Fitted elemental-phase reference energies. Phys Rev B 2012;85:115104. URL: https://doi.org/10.1103/PhysRevB.85.115104.

[73] Gorai, P., McKinney, R.W., Haegel, N.M., Zakutayev, A., Stevanovic, V.. A computational survey of semiconductors for power

electronics. Energy & Environmental Science 2019;12(11):3338–3347. URL: https://doi.org/10.1039/C9EE01529A.

[74] Qu, J., Stevanović, V., Ertekin, E., Gorai, P.. Doping by design: finding new n-type dopable ABX_4 zintl phases for thermoelectrics. J Mater Chem A 2020;8(47):25306. URL: https://doi.org/10.1039/D0TA08238D.

[75] Peng, H., Scanlon, D.O., Stevanovic, V., Vidal, J., Watson, G.W., Lany, S.. Convergence of density and hybrid functional defect calculations for compound semiconductors. Phys Rev B 2013;88:115201. URL: https://doi.org/10.1103/PhysRevB.88.115201.

[76] Wei, S., Zunger, A.. Band offsets at the $CdSCuInSe_2$ heterojunction. Applied Physics Letters 1993;63(18):2549–2551. URL: https://doi.org/10.1063/1.110429.

[77] Vidal, J., Lany, S., d'Avezac, M., Zunger, A., Zakutayev, A., Francis, J., et al. Band-structure, optical properties, and defect physics of the photovoltaic semiconductor SnS. Applied Physics Letters 2012;100(3):032104. URL: https://doi.org/10.1063/1.3675880.

[78] Scanlon, D.O., Dunnill, C.W., Buckeridge, J., Shevlin, S.A., Logsdail, A.J., Woodley, S.M., et al. Band alignment of rutile and anatase TiO_2. Nature Mater 2013;12(9):798–801. URL: https://doi.org/10.1038/nmat3697.

[79] Lany, S., Zunger, A.. Assessment of correction methods for the band-gap problem and for finite-size effects in supercell defect calculations: Case studies for ZnO and GaAs. Phys Rev B 2008;78(23):235104. URL: https://doi.org/10.1103/PhysRevB.78.235104.

[80] Toriyama, M.Y., Qu, J., Snyder, G.J., Gorai, P.. Defect chemistry and doping of BiCuSeO. J Mater Chem A 2021;9:20685–20694. URL: http://doi.org/10.1039/D1TA05112A.

[81] Lany, S., Zunger, A.. Accurate prediction of defect properties in density functional supercell calculations. Model Simul Mater Sc 2009;17(8):084002. URL: https://doi.org/10.1088/0965-0393/17/8/084002.

[82] Goyal, A., Gorai, P., Peng, H., Lany, S., Stevanović, V.. A computational framework for automation of point defect calculations. Comp Mater Sci 2017;130:1. URL: https://doi.org/10.1016/j.commatsci.2016.12.040.